

# *In Situ* Observation of Kinetic Processes of Lath Bainite Nucleation and Growth by Laser Scanning Confocal Microscope in Reheated Weld Metals



GAOJUN MAO, RUI CAO, XILI GUO, YONG JIANG, and JIANHONG CHEN

The kinetic processes of nucleation and growth of bainite laths in reheated weld metals are observed and analyzed by a combination of a laser confocal scanning microscope and an electron backscattering diffraction with a field emission scanning electron microscope. The results indicate that the surface relief induced by phase transformation is able to reveal the real microstructural morphologies of bainite laths when viewed from various angles. Five nucleation modes and six types of growth behaviors of bainite laths are revealed. The bainite lath growth rates are measured to vary over a wide range, from 2  $\mu\text{m/s}$  to higher than 2000  $\mu\text{m/s}$ . The orientations of the bainite laths within a prior austenite grain are examined and denoted as different variants. On the basis of variant identification, the reason is analyzed for various growth rates which are demonstrated to be affected by (1) the density of the high-angle misorientation in it, (2) the included angle between habit planes of different variants, and (3) the direction of lath growth with respect to the free (polished) surface.

DOI: 10.1007/s11661-017-4348-7

© The Minerals, Metals & Materials Society and ASM International 2017

## I. INTRODUCTION

TO satisfy the increasing demand for high strength and excellent toughness of steel in the automotive and structural industries, bainite microstructure has illustrated its vital importance in recent years.<sup>[1–3]</sup> In the past decades, the bainite morphology could only be detected after phase transformation by conventional metallographic investigations. In recent years, the continuous nucleation and growth process of bainite has been studied by transmission electron microscope (TEM) and other instruments. Bhadeshia *et al.* measured the lengthening rate of the subunit of bainite sheaf as 75  $\mu\text{m/s}$  by a photoemission electron microscope.<sup>[4]</sup> Kang *et al.* provided direct evidence for bainite growth through *in situ* observation of the growth process of bainite by TEM with a hot stage under isothermal conditions.<sup>[5]</sup> Li *et al.* conducted

phase transformation behavior in a Ti-50.8 at. pct Ni alloy by *in situ* TEM observation.<sup>[6]</sup> In recent years, a powerful method for bainite transformation analysis, *i.e.*, *in situ* observation by a high-temperature laser scanning confocal microscope (LSCM) with an infrared imaging furnace, has been used to analyze the morphological evolution during the cooling process.<sup>[7,8]</sup> LSCM makes it possible to observe the continuous processes of bainite transformation. This *in situ* observation of bainite nucleation and growth is based on the relief phenomenon of the new phase produced during phase transformation due to volume change resulted from lattice change.<sup>[7]</sup>

Hu *et al.* carried out dynamic observation of bainite transformation in a Fe-C-Mn-Si super bainite steel by LSCM. They concluded that bainite growth had the features of interlocking and impingement of bainitic platelets.<sup>[7]</sup> Zhang *et al.* investigated the effect of cooling rate on phase transformation in the low-carbon B-treated steel through LSCM. It showed that the typical transformation products in the low-carbon B-treated steels are the microstructures including intragranular bainitic ferrite, nucleated entirely in the austenite grain.<sup>[8]</sup> They confirmed the findings that had previously been revealed by Ishikawa and Takahashi.<sup>[9]</sup> Xu *et al.* observed the nucleation and morphological evolution in a super bainite steel by LSCM. They found that bainite growth was characterized by the impingement of bainite sheaves, which resulted in an interlocked bainite microstructure.<sup>[10]</sup>

---

GAOJUN MAO, RUI CAO, and JIANHONG CHEN are with the Department of Materials Science and Engineering, Lanzhou University of Technology, Lanzhou 730050, China and also with the State Key Laboratory of Advanced Processing and Recycling of Non-ferrous Metals, Lanzhou University of Technology, Lanzhou 730050, China. Contact e-mail: zchen@lut.cn XILI GUO and YONG JIANG are with Atlantic China Welding Consumables, Inc., Zigong 643000, China.

Manuscript submitted January 24, 2017.

Article published online October 11, 2017

Additionally, analytical investigation of bainite nucleation and growth has been conducted by Zhang *et al.* They investigated the morphological and crystallographic evolution of bainite transformation in Fe-0.15C binary alloy by LSCM. Their results indicated that the bainitic ferrite was nucleated at the grain boundary and inclusion, and that the secondary bainitic ferrite was sympathetically nucleated at the broad side of the primary bainitic ferrites followed by the impingement of the bainitic ferrite between the secondary bainitic ferrites.<sup>[11]</sup> Zhang *et al.* analyzed the dependence of toughness on the prior austenite grain size in steel weld metal by LSCM. Three nucleation sites of bainite at the micrometer scale were revealed, which were the grain boundaries, the inclusions on grain boundary where primary bainitic ferrite was nucleated, and the surface of the primary bainitic ferrite where sympathetic nucleation occurred.<sup>[12]</sup> Yada *et al.* investigated the growth of typical upper and lower bainite observed under LSCM. They used a cine camera film with 24 frames/s and found that the plate length linearly increased with time.<sup>[13]</sup> Kolmskog *et al.* directly observed that bainite could also grow below Ms by using LSCM. In this temperature region, some units of bainite grow slowly, while at the same time another series of units suddenly appear and grow rapidly one by one.<sup>[14]</sup>

An electron backscattered diffraction (EBSD) technique also plays a crucial role to better understand the crystallography of bainite. It is possible to determine the orientation of a bainite sheaf by using an orientation imaging microscope (OIM) after obtaining the EBSD map<sup>[15]</sup> with a scanning electron microscope (SEM).<sup>[16,17]</sup> Terasaki *et al.* investigated the morphology and crystallography of bainite transformation in a single

prior austenite grain of low-carbon steel by combining LSCM and EBSD. They revealed that variants of the bainitic ferrite belonging to the same Bain zone were synchronized in terms of phase transformation, although they were separated from each other by another Bain zone.<sup>[16]</sup> Sarizam *et al.* analyzed the effects of holding temperature on bainite transformation in Cr-Mo steel by combining LSCM and EBSD. They discovered the following facts: (1) the nucleation of the bainitic ferrite block mainly initiated from the austenite grain boundary, (2) the formation of the same variant pairs and different variant pairs in a block proved the mechanism of variant preferential selection during bainite transformation, which caused the formation of a coarser block, especially at the higher holding temperature, and (3) the packet boundary is connected with a low misorientation angle variant belonging to the same Bain zone.<sup>[17]</sup>

Nevertheless, the dynamic process of bainite growth (direction, rate, *etc.*) and crystallographic features remain unclear. In this study, the dynamic process of nucleation and growth of bainite sheaves were observed *in situ*. The crystallographic analyses including variants calibration and orientation calculation were conducted through a combination of LSCM and EBSD in the same field of view to thoroughly understand the bainite transformation mechanism.

## II. EXPERIMENTAL PROCEDURE

### A. Materials and Specimens

The test materials were low-carbon bainite weld metals, the compositions of which are shown in Table I. The multilayer weld metals were produced using the

**Table I. Chemical Compositions of the Weld Metal (Weight Percent)**

Specimen	C	Mn	Si	S + P	Cr	Mo	Ni	V + Cu	Fe
Ni6	0.052	1.52	0.35	0.02	0.7	0.75	5.9	0.02	balance
Ni7	0.052	1.53	0.35	0.02	0.8	0.7	6.98	0.02	balance

**Table II. Specimens and Corresponding Experiment Procedures**

Specimen	Heating Process	Isothermal Holding	Cooling Process	Isothermal Holding	Cooling Process
Ni6-1	Heated to 473 K (200 °C) at 0.8 K/s, and then heated to 1623 K (1350 °C) at 5 K/s	At 1623 K (1350 °C) for 4 min	Cooled to 873 K (600 °C) at 5 K/s, and then cooled to 573 K (300 °C) at 0.2 K/s	—	Cooled to 293 K (20 °C) (room temperature) at the rate of 5 K/s
Ni6-2	—	—	Cooled to 723 K (450 °C) at 5 K/s	At 723 K (450 °C) for 40 min	—
Ni6-3	—	—	Cooled to 713 K (440 °C) at 5 K/s	At 713 K (440 °C) for 10 min	—
Ni7-1	—	—	—	—	—
Ni7-2	—	—	Cooled to 1073 K (800 °C) at 5 K/s, and then cooled to 573 K (300 °C) at 1 K/s	—	—

metal-cored wire with the diameter of 1.6 mm as the filler metal. A Y-type groove was cut on a plane steel plate with dimensions of 450 × 250 × 28 mm as shown in Figure 1(a). The observed specimens in the LSCM were cut from the weld metal and machined to a cylinder of 6 mm in diameter and 2 mm in height (shown in the left side of Figure 1(a)). The top and bottom surfaces of LSCM specimens were polished conventionally to keep a smooth measured surface.

### B. Device and Procedure

The investigations were conducted in an LSCM (Laser Tec VL2000DX-SVF17SP Yonekura Manufacturing Co., Ltd., Kanagawa, Japan). This LSCM is schematically shown in Figure 1(b). The specimens were put in an alumina crucible, which was heated and cooled in a vacuum chamber filled with argon. The laser light was focused and scanned at the specimen surface. The successive images were taken at an interval of 0.03 to 0.07 seconds and were collected by a CCD camera.

Figure 1(c) shows the heating and cooling cycles for LSCM observations. The detailed experimental procedures are presented in Table II.

All specimens were heated to 473 K (200 °C) at the rate of 0.8 K/s, then heated to the austenitizing temperature of 1623 K (1350 °C) at 5 K/s and held there for 4 minutes. Subsequently, the Ni6-1 specimen was immediately cooled to 873 K (600 °C) at 5 K/s, followed by cooling to 573 K (300 °C) at 0.2 K/s, where bainite transformation was finished, and then it was cooled to room temperature. The Ni6-2 specimen was cooled to 723 K (450 °C) at 5 K/s and then was subjected to an isothermal treatment at 723 K (450 °C) for 40 minutes to obtain the genuine structure including bainite and untransformed austenite, and finally it was cooled to room temperature. The Ni6-3 specimen was cooled to 713 K (440 °C) at 5 K/s, then subjected to an isothermal treatment at 713 K (440 °C) for 10 minutes, and finally cooled to room temperature. The Ni7-1 specimen was cooled to room temperature at 5 K/s, and the Ni7-2 specimen was immediately cooled to 1073 K (800 °C) at

5 K/s, then was cooled at 1 K/s to 573 K (300 °C), and finally cooled to room temperature. An atomic force microscope (AFM) (TI950 Tribo Indenter), which is capable of making high-resolution observation and measurement of surface topography, was utilized to examine the surface relief caused by the formation of bainite laths. EBSD measurements were conducted in the same field of view on an SEM (FEI Quanta™ 450 FEG; Hillsboro, OR). An orientation (OR) imaging of the SEM–EBSD data was performed with a 250 nm step size. TSL-OIM™ (EDAX; Mahwah, NJ) software was used to measure and analyze the OR. The OR of bainite with respect to the parent  $\gamma$  was determined by a method reported previously.<sup>[18]</sup> Although the measured OR deviated slightly from the exact K–S OR, as described later, the deviation angles were small enough to apply Table III to index variants.<sup>[19]</sup>

## III. RESULTS AND DISCUSSION

### A. Surface Relief Morphology and Microstructure

Ko and Cottrell first observed the relief phenomenon of bainite transformation in 1952, and the principle they used for *in situ* observation of bainite nucleation and growth was based on the relief phenomenon occurring in phase transformation.<sup>[20]</sup> Figure 2(a) shows the features of the specimen surface after the LSCM experiment. The surface relief of the transformed specimen was completely copied by the thin oxide skin, and it reflected the bainite transformation features. Three main morphologies are displayed in Figure 2(a): (1) white lath stripes—these are enclosed by a blue line, (2) flatter and darker facets showing the side plane of the sloping laths—these are enclosed by red lines, and (3) sloping laths—these are enclosed by green lines. Accordingly, three corresponding morphologies of microstructure are shown in Figure 2(b). These morphologies were observed using an SEM after the specimen was etched with a 3 pct nital solution. The narrow strips of lath bainite marked with an A in Figure 2(b) are consistent

Table III. Twenty-Four Variants of K–S Relationship<sup>[18]</sup>

Variant No.	Plane Parallel ( $\gamma$ )/( $\alpha$ )	Direction Parallel [ $\gamma$ ]/[ $\alpha$ ]	Misorientation from V1 (deg)	Variant No.	Plane Parallel ( $\gamma$ )/( $\alpha$ )	Direction Parallel [ $\gamma$ ]/[ $\alpha$ ]	Misorientation from V1 (deg)
1	(111)/(011)	$\bar{1}01$ // $\bar{1}\bar{1}\bar{1}$	—	13	( $\bar{1}11$ )/(011)	$0\bar{1}\bar{1}$ // $\bar{1}\bar{1}\bar{1}$	14.88
2		$\bar{1}0\bar{1}$ // $\bar{1}\bar{1}\bar{1}$	60.00	14		$0\bar{1}\bar{1}$ // $\bar{1}\bar{1}\bar{1}$	50.51
3		$0\bar{1}\bar{1}$ // $\bar{1}\bar{1}\bar{1}$	60.00	15		$\bar{1}0\bar{1}$ // $\bar{1}\bar{1}\bar{1}$	57.21
4		$0\bar{1}\bar{1}$ // $\bar{1}\bar{1}\bar{1}$	10.53	16		$\bar{1}0\bar{1}$ // $\bar{1}\bar{1}\bar{1}$	20.61
5		$\bar{1}\bar{1}0$ // $\bar{1}\bar{1}\bar{1}$	60.00	17		$\bar{1}10$ // $\bar{1}\bar{1}\bar{1}$	51.73
6		$\bar{1}\bar{1}0$ // $\bar{1}\bar{1}\bar{1}$	49.47	18		$\bar{1}10$ // $\bar{1}\bar{1}\bar{1}$	47.11
7		$\bar{1}0\bar{1}$ // $\bar{1}\bar{1}\bar{1}$	49.47	19		$\bar{1}10$ // $\bar{1}\bar{1}\bar{1}$	50.51
8		$\bar{1}0\bar{1}$ // $\bar{1}\bar{1}\bar{1}$	10.53	20		$\bar{1}10$ // $\bar{1}\bar{1}\bar{1}$	57.21
9		$\bar{1}\bar{1}0$ // $\bar{1}\bar{1}\bar{1}$	50.51	21		$0\bar{1}\bar{1}$ // $\bar{1}\bar{1}\bar{1}$	20.61
10	( $\bar{1}\bar{1}1$ )/(011)	$\bar{1}\bar{1}0$ // $\bar{1}\bar{1}\bar{1}$	50.51	22		$0\bar{1}\bar{1}$ // $\bar{1}\bar{1}\bar{1}$	47.11
11		$0\bar{1}\bar{1}$ // $\bar{1}\bar{1}\bar{1}$	14.88	23		$\bar{1}0\bar{1}$ // $\bar{1}\bar{1}\bar{1}$	57.21
12		$0\bar{1}\bar{1}$ // $\bar{1}\bar{1}\bar{1}$	57.21	24		$\bar{1}0\bar{1}$ // $\bar{1}\bar{1}\bar{1}$	21.06

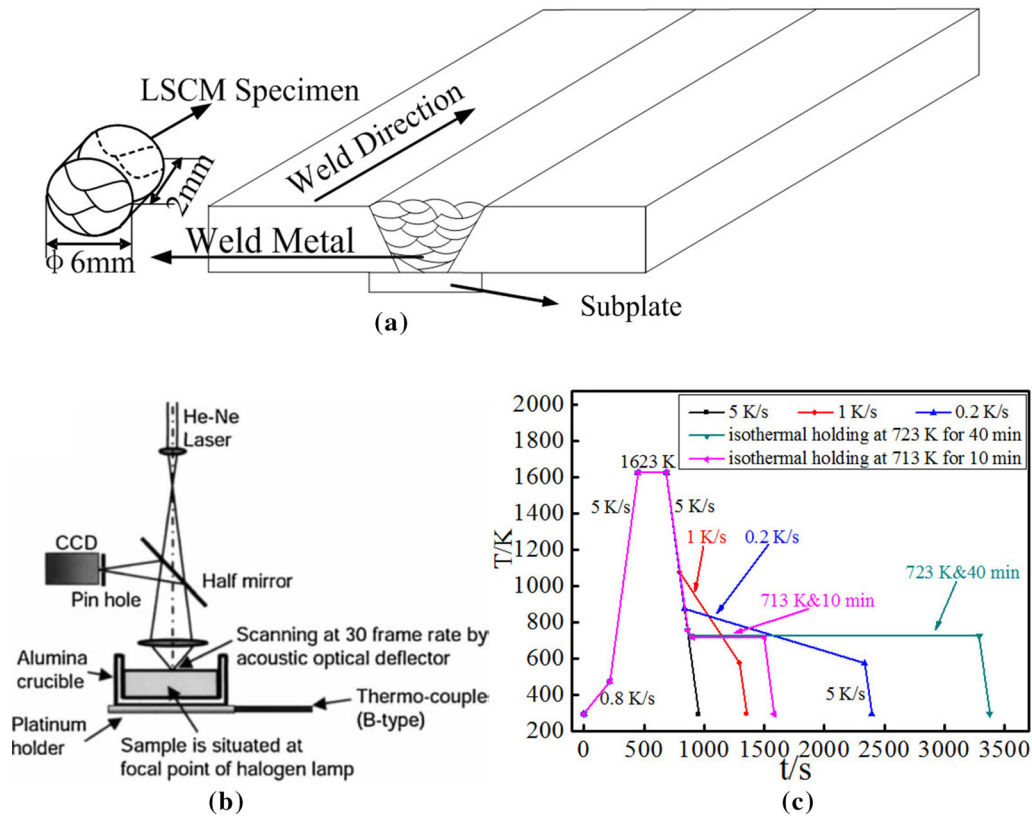


Fig. 1—(a) Schematic illustration of LSCM specimen cut from the Y-type joint by multipass welding; (b) schematic illustration of the optical system in a high-temperature laser scanning confocal microscope; and (c) curves of thermal cycles applied to the specimens for LSCM experiments.

with white stripes enclosed by a blue line in Figure 2(a). Likewise, the slightly wider strips of lath bainite marked with a B in Figure 2(b) are consistent with the sloping laths enclosed by green lines in Figure 2(a). The flatter and darker facets appearing among lath bainite blocks marked with C in Figure 2(b) also correspond to the flatter and darker facets enclosed by red lines in Figure 2(a). That is, the flatter and darker facets in Figure 2(a) are the side planes of a lath bainite packet.

Figure 3 displays a highly magnified image of the tent-shaped relief of bainite laths (a) and the morphology of the surface relief taken by AFM (b and c). From the relief, we can calculate the strain caused by phase transformation. As shown in Figures 3(b) and (c), the strain is taken as the quotient of the height divided by the width of the tent-shaped relief.<sup>[21]</sup> From the relief in Figure 3(a), the bainite transformation strain is calculated to be around 0.2.

The schematic diagram in Figure 3(d) shows three possible angles by which the polished observing surfaces cut through the bainite laths. The three cutting angles cause various relief features to be seen because of the various directions of the broad side of the bainite lath related to the polished observing surface.

- (i) When the broad side plate of bainite laths is perpendicular to the polished (observed) surface (surface A in Figure 3(d)), the surface relief and

microstructural morphology will be the slim strips, as shown in the region enclosed by a blue line in Figures 2(a) and (b).

- (ii) When the broad side plate of bainite laths is inclining with an acute angle toward the polished surface (surface B in Figure 3(d)), the surface relief and microstructural morphology will manifest itself as sloping laths and slightly wider strips, as shown in the regions enclosed by green lines in Figures 2(a) and (b).
- (iii) When the broad side plate of bainite laths remains parallel to the polished surface (surface C in Figure 3(d)), the surface relief and microstructural morphology will be presented as flatter and darker facets, as shown in the regions enclosed by red lines in Figures 2(a) and (b).

These flatter and darker facets (Figure 2(a)) have been referred to as coalesced bainite, evolving by the coalescence of finer bainite platelets, each of which is separately nucleated but in the same crystallographic orientation during prolonged growth.<sup>[22]</sup> However, in present work the flatter and darker facets are identified as the broad side planes of lath bainite packets. It should be noted that all figures with images of relief were taken by LSCM directly without oxide film except Figures 2(a) and 3(a).

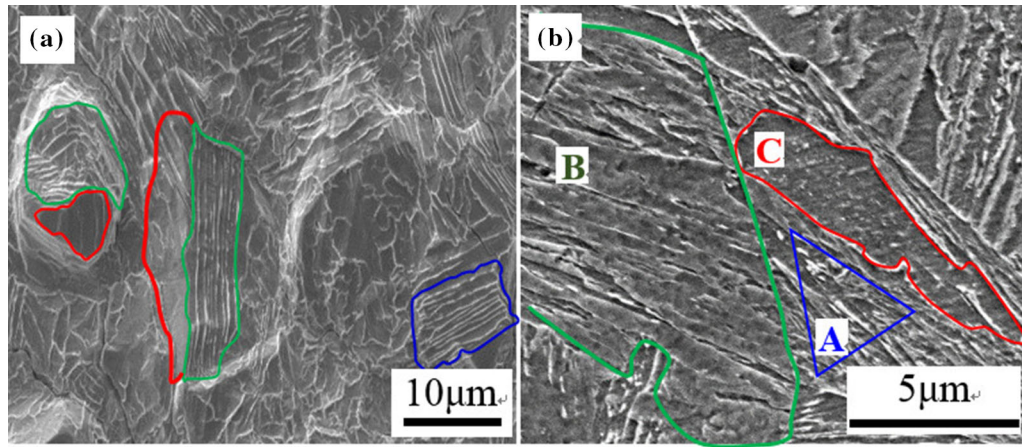


Fig. 2—(a) Surface relief morphology and (b) microstructural morphology—(A) blue lines enclose white lath stripes; (B) red lines enclose flatter and darker facets; (C) green lines enclose sloping laths.

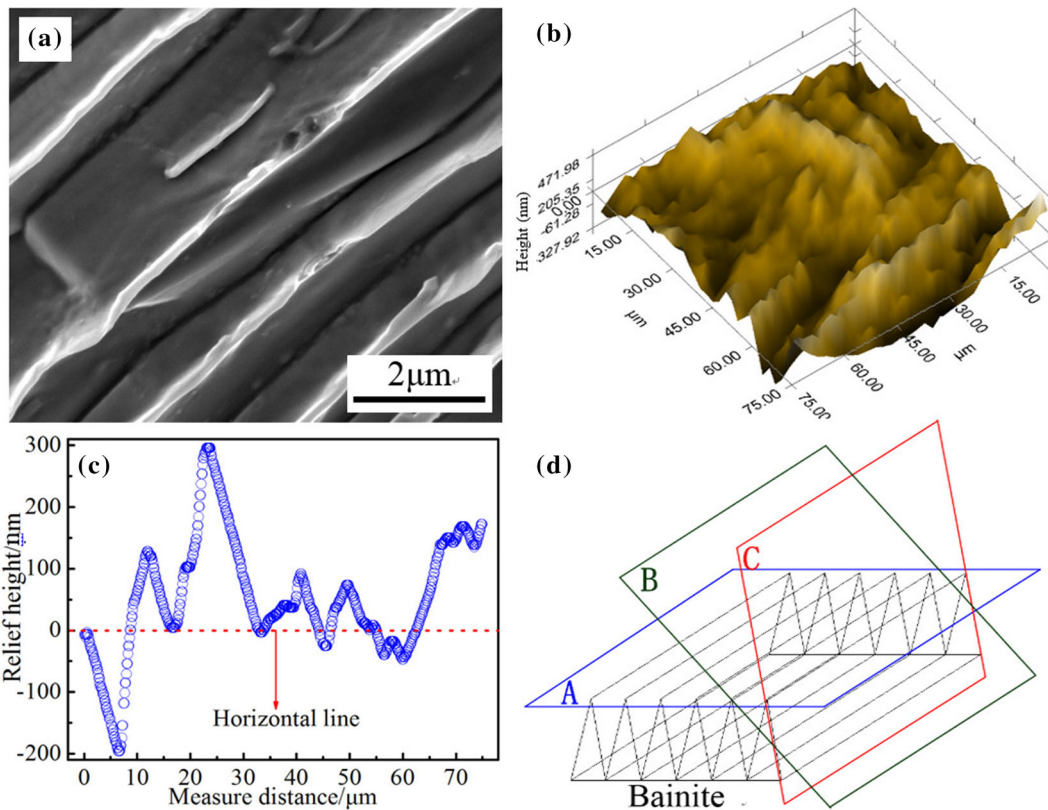


Fig. 3—(a) Tent-shaped relief of bainite laths; (b) AFM images showing surface relief; (c) AFM scans showing surface relief; (d) schematic diagram of tent-shaped bainite laths—surfaces A, B, and C indicate polished surfaces at different directions.

### B. *In Situ* Observation of Nucleation of Bainite

There are many crystal defects in the austenite matrix in places such as grain boundary, subgrain boundary, twin boundary, inclusion, dislocation, and stacking fault. Around these crystal defects the distortion energy is higher.<sup>[23]</sup> Thus, the bainite laths easily nucleate around these sites.

Xu, Jin, and Zhang ranked all possible nucleation sites in order of decreasing difficulty: the homogeneous nucleation on free surface, the vacancy nucleation, the

dislocation nucleation, the stacking fault nucleation, the grain boundary nucleation, and the phase boundary nucleation.<sup>[24]</sup>

For the Ni7-2 specimen, at a cooling rate of 1 K/s (see Table II), five nucleation modes were revealed and are displayed in Figure 4 as follows:

- (i) A single point of nucleation first occurred on the grain boundary shown in Figures 4(a) through (d). After a short growth, by its side a subsequent nucleus appeared and grew parallel

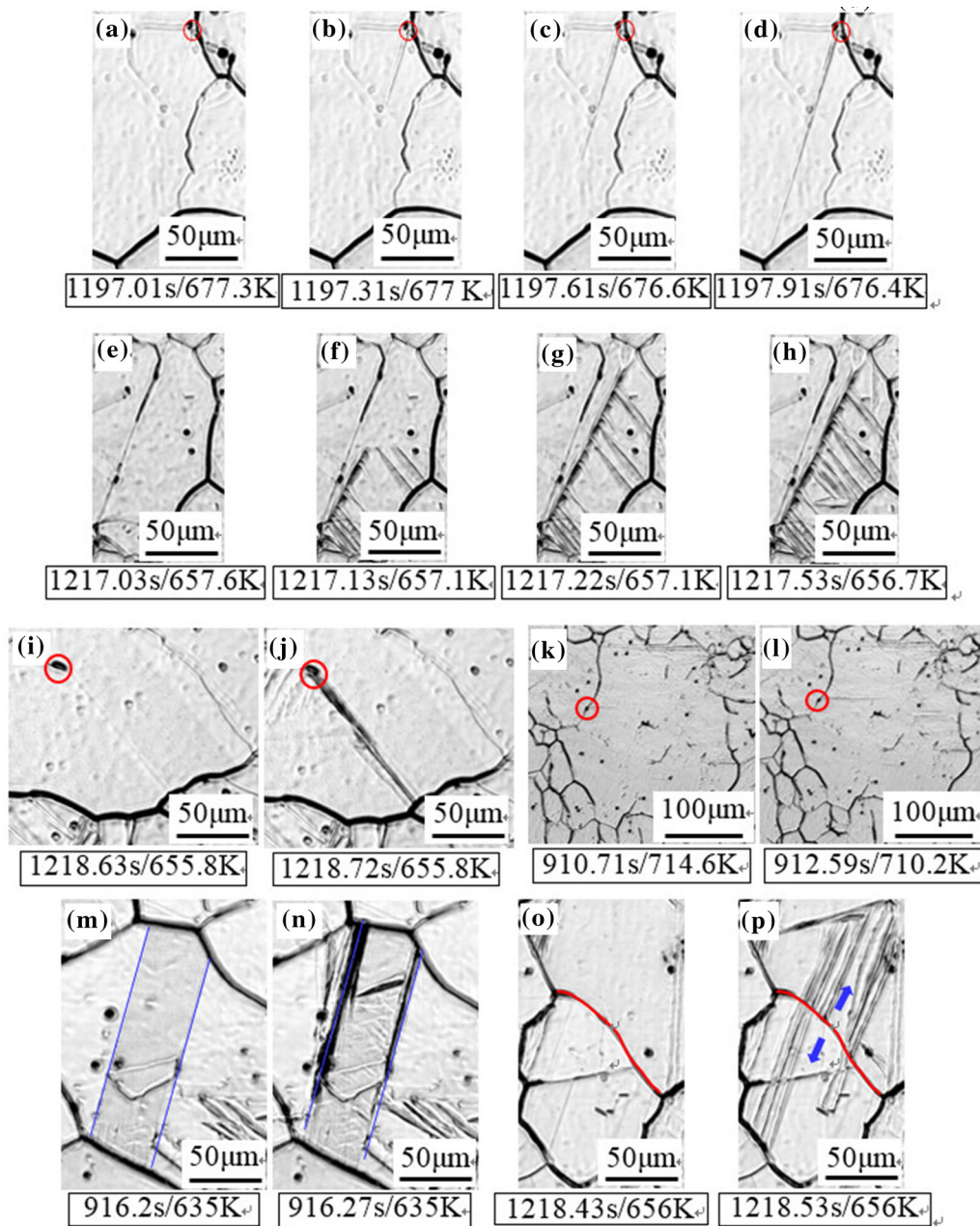


Fig. 4—Observation of various nucleation sites: (i) (*a* through *d*) single-point nucleation and growth to the opposite grain boundary, (the nucleation site is indicated by red circle); (ii) (*e* through *h*) sympathetic nucleation on one broad side of a just created bainite lath; (iii) (*i*) and (*j*) nucleation at the inclusions inside a grain (the inclusion is enclosed by red circles); (*k*) and (*l*) nucleation at the inclusions on the grain boundary; (iv) (*m*) and (*n*) nucleation on two boundaries of a twin band (the twin boundaries are indicated by blue lines); (v) (*o*) and (*p*) simultaneous nucleation on both sides of a grain boundary (the grain boundary is indicated by the red line and the growth directions of newly formed bainite sheaves are indicated by two blue arrows).

to the first lath. Both laths grew in a straight line into the grain at an angle of 40 deg inclined to the grain boundary. This shows that in cases where there have not been bainite laths previously formed, the boundary of the austenite grain is the first selected site for nucleation.

- (ii) As shown in Figures 4(*e*) through (*h*), sympathetic nucleation of numerous bainite laths occurred on the broad side of a just created bainite lath (the lath in Figures 4(*f*) through (*g*))

that grows from the bottom left to the top right). The occurrence of numerous bainite lath nucleations implies that the bainite lath boundary is the favorite site for nucleation. This shows that the crystallographic orientation of the broad side of the preformed bainite lath is the favorite location for the nucleation of the successive accommodating laths.<sup>[25]</sup>

- (iii) Nucleation occurred at the inclusions or other defects inside a grain. Inclusions and other

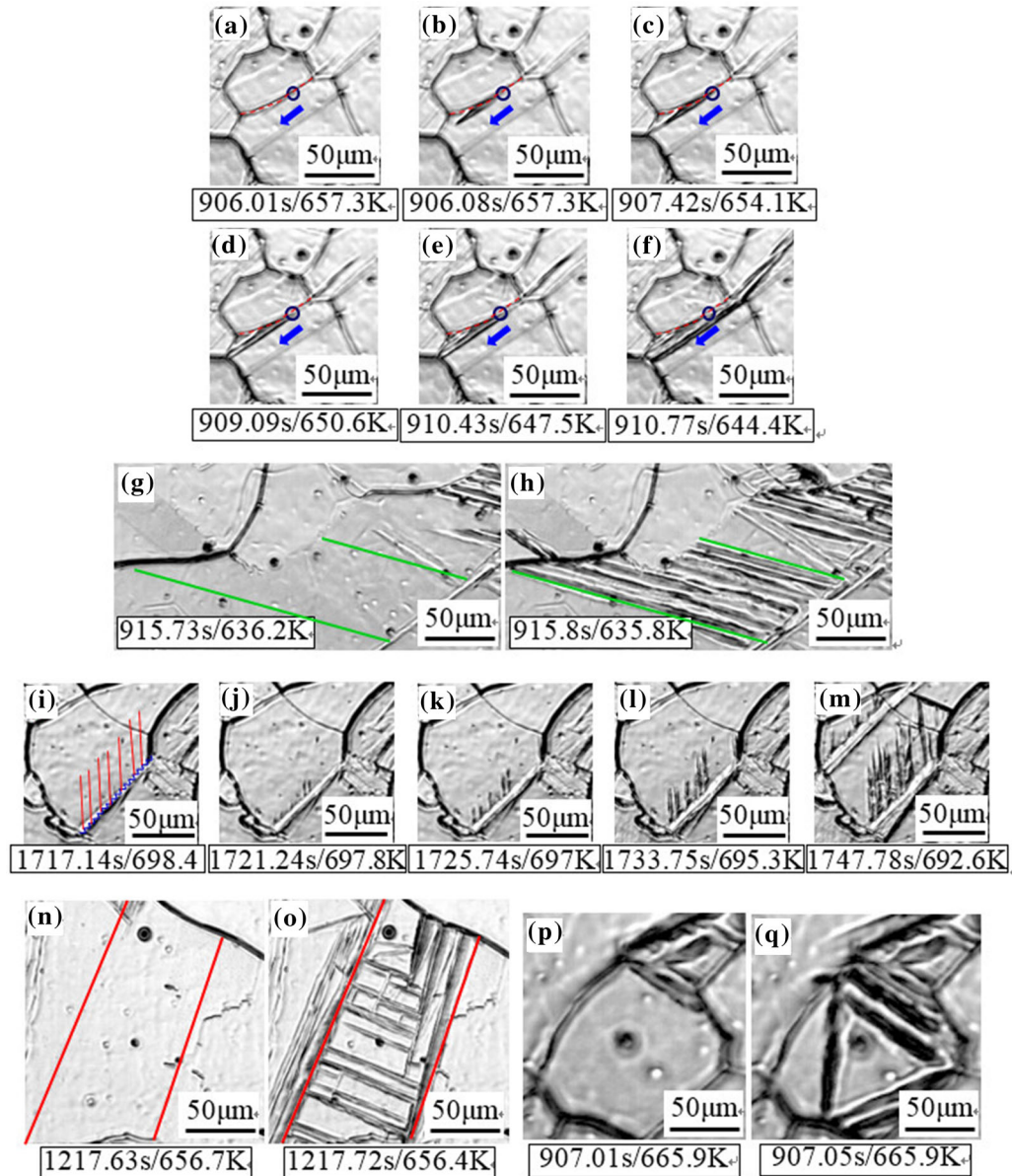


Fig. 5—Observation of various growth modes: (ii) (a through f) a single lath growing along a grain boundary; (iii) (g) and (h) a number of parallel bainite laths simultaneously nucleating and growing fast from the broad side of a just created bainite lath with an inclined angle of 60 deg—they are growing in the zone indicated by two green lines; (iv) (i through m) a number of bainite laths growing parallel to each other at very low rate; (v) (n) and (o) a latticed frame nucleating and growing in the zone indicated by two red lines; (vi) (p) and (q) a triangle latticed frame simultaneously nucleating and growing.

defects inside a grain also acted as nucleation sites, and these are indicated by a red circle in Figures 4(i) through (j) and 9(a) and (b). This can be explained by the idea that the coherent or semi-coherent interface between inclusions/ferrite<sup>[26]</sup> and the high strain energy due to different thermal expansion coefficient between inclusions and austenite<sup>[26]</sup> make the nucleation easy. Some bainitic ferrites were also nucleated at the inclusions on the grain boundary and grew into the austenite grain (indicated by a red circle in Figures 4(k) through (l)).

(iv) Nucleation occurred on twin boundaries. As

shown in Figures 4(m) through (n), bainite laths were nucleated along twin boundaries (indicated by two blue lines). Because the interface energy of the annealing twin is lower than that of grain boundary,<sup>[24]</sup> although twin boundaries also act as sites for bainite to nucleate, the bainite nucleation along twin boundaries occurs at lower temperatures such as 625 K (362 °C).

(v) Simultaneous nucleation occurred on both sides of a grain boundary. As shown in Figures 4(o) and (p), bainite laths were nucleated on both sides of a grain boundary and then extended into both grains.

### C. In Situ Observations of the Growth of Bainite Laths

Six kinds of bainite lath growth modes were observed *in situ*: (i) successive single laths growing straight into a grain (Figures 4(a) through (d)), (ii) a single lath growing along a grain boundary (Figures 5(a) through (f)), (iii) a number of nuclei simultaneously growing in parallel at a high rate in a grain (Figures 5(g) and (h)), (iv) a number of nuclei successively growing at a very low rate in a grain and growing parallel to each other (Figures 5(i) through (m)), (v) laths simultaneously growing in different directions and forming a latticed frame (Figures 5(n) and (o)), and (vi) simultaneous nucleation and growth of a triangle latticed frame (Figures 5(p) and (q)). These growth modes are described below:

- (i) As shown in Figures 4(a) through (d), for the Ni7-2 specimen in Table II, one single bainite lath was nucleated at the grain boundary and grew in a direction of 40 deg inclined to it and reached the opposite grain boundary. The bainite lath length of about 165  $\mu\text{m}$  increased linearly at a time interval of 0.9 seconds at a rate of 183  $\mu\text{m/s}$ .
- (ii) As shown in Figures 5(a) through (c), one bainite lath was nucleated at the grain boundary and grew along the boundary at a rate of about 43  $\mu\text{m/s}$ . Likewise, another bainite lath was attached to the primary bainite lath and grew at a rate of about 48  $\mu\text{m/s}$  as shown in Figures 5(d) through (f).
- (iii) As shown in Figures 5(g) and (h), for the Ni7-1 specimen at the cooling rate of 5 K/s shown in Table II, a number of parallel bainite laths were simultaneously nucleated and grew fast from the broad side of a just created bainite lath with an inclined angle of 60 deg. Final bainite laths can be observed in the zone indicated by two green lines. The bainite laths extended very fast to a length of 200  $\mu\text{m}$  in less than 0.1 seconds at a rate of 2244.3  $\mu\text{m/s}$ .
- (iv) As shown in Figures 5(i) through (m), for the Ni6-1 specimen cooled at 0.2 K/s shown in

Table II, the parallel growth of a number of bainite laths was completed over a wide temperature range ( $-6$  K) and a long time period ( $+30$  seconds). The average growth rate of individual bainite laths was around 2.25  $\mu\text{m/s}$ .

- (v) It is revealed in Figures 5(n) and (o) that the bainite laths simultaneously grew in different directions and formed a latticed frame within a time interval of only 0.09 seconds.
- (vi) As shown in Figures 5(p) and (q), a triangle latticed frame formed by the simultaneous growth of bainite laths within 0.04 seconds. The 60 deg between the three sides of the triangle is consistent with the included angle between the crystal directions of [110], [101], and [011] in an austenite crystal cell.

### D. Characteristics of the Growth of Bainite Laths

Five characteristics were discovered in the growth of bainite laths:

- (1) A large difference appears in the growth rates of the bainite laths. Figure 6(a) shows three typical growth rates observed in the Ni7-2 specimen cooled at 5 and 1 K/s, and the Ni6-1 specimen cooled at 0.2 K/s. The average growth rate for each was 1979, 183, and 2.25  $\mu\text{m/s}$ , respectively. Figures 6(b) and (c) display the detailed measurement results of Figure 6(a) line (iii), *i.e.*, the growing mode (iii), and Figure 6(a) line (iv), *i.e.*, the growing mode (iv), respectively. In these figures, the great difference in growth rates can be attributed to the greater difference in cooling rates and thus to the degree of the supercooling. However, there is one case in an austenite grain where the growth rates of bainite laths are apparently different from each other even though their transformations occurred at the same temperature. This case will be analyzed in the next section.
- (2) A large difference appears in the start time of nucleation and growth of bainite laths. For the Ni6-2 specimen, a typical nucleation and growth

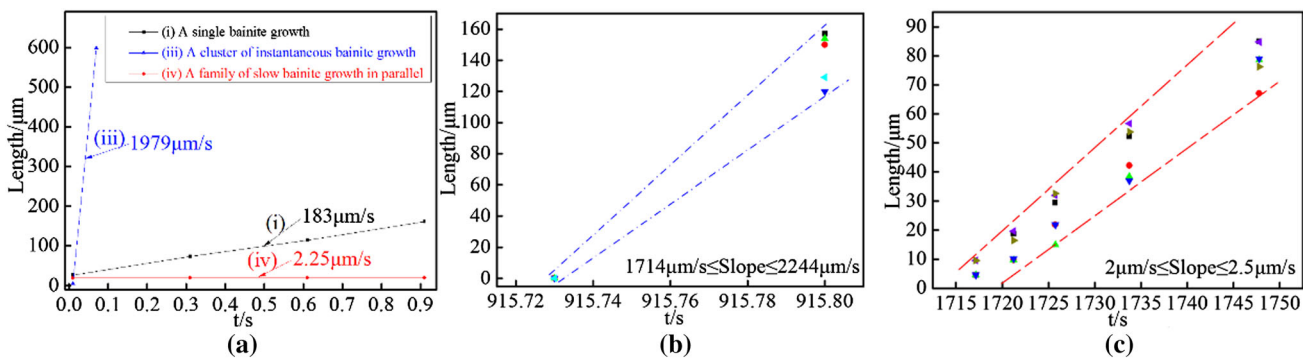


Fig. 6—(a) Plot of growing length against time for three typical growth modes at various average rates; (b) plot of growing length against time for the growing mode (iii), *i.e.*, parallel bainite laths simultaneously nucleating and growing fast; (c) plot of average length against time for growing mode (iv), *i.e.*, growing slowly and in parallel to each other.



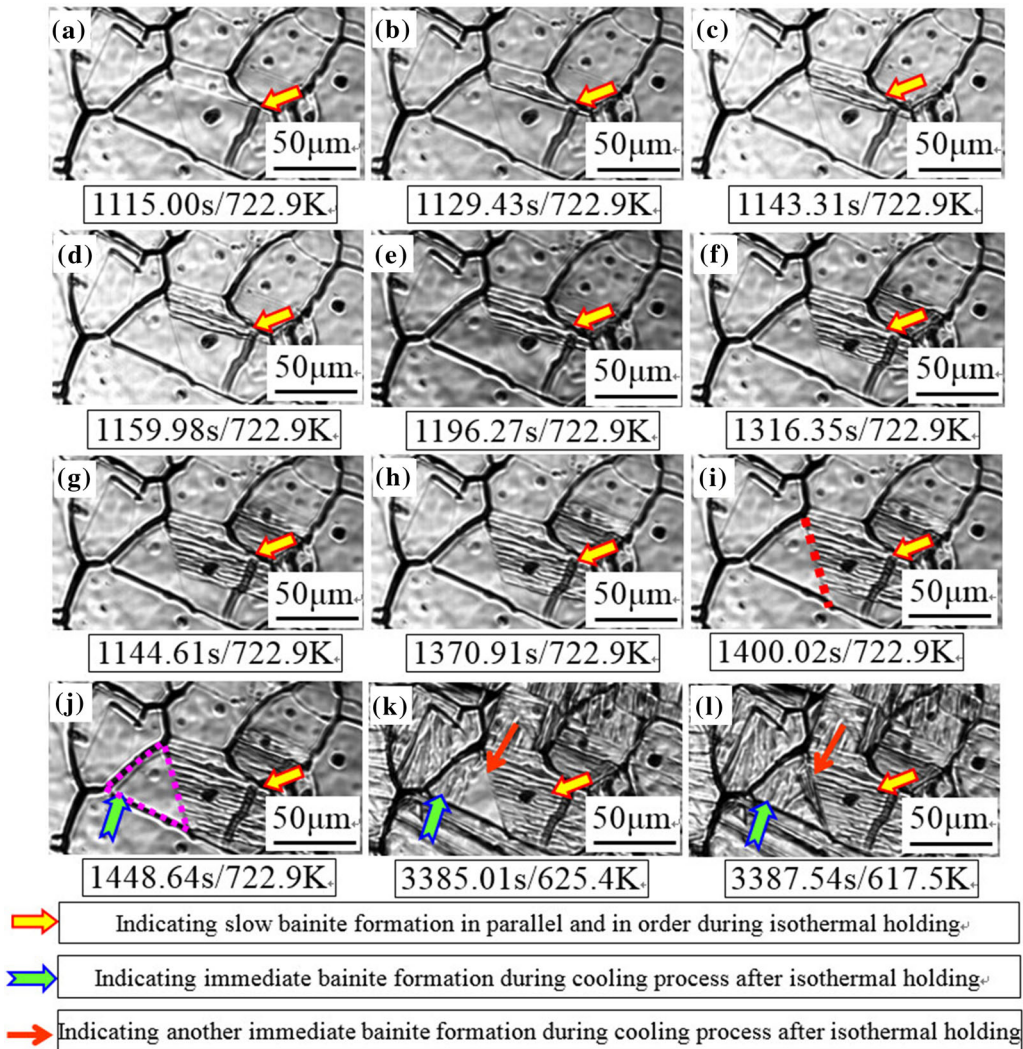


Fig. 7—Observation of the start temperatures and time of bainite nucleation and growth: (a through j) the process of bainite laths nucleating on the boundary, growing in parallel in the interior of the studied grain and stopping on the subgrain boundary (the subgrain boundary is indicated by a red dotted line in (i)) during isothermal holding at 722.9 K (449.9 °C); (k) immediate bainite formation of one group of bainite laths in the left flat triangle zone (indicated by a pink dotted triangle) during cooling process after isothermal holding; (l) formation of another group of bainite immediately adjacent to the subgrain boundary during the cooling process.

process is depicted in Figure 7. As shown in Figures 7(a) through (g), parallel bainite laths successively formed one by one gradually (indicated by yellow arrows in Figure 7). In this typical process, it took 15 seconds for each bainite lath to finish growth as shown in Figures 7(a) through (d). However, when an inclusion or void was encountered by a bainite lath, the growth rate dropped considerably and it took 120 seconds for one lath to grow as shown in Figures 7(e) and (f). Finally, the bainite laths stopped at the spots forming a red dotted straight line in Figures 7(i) and (j) and left a flatter triangle region (this region is enclosed by a pink dotted line). The red dotted line formed by red spots appears to be a subgrain boundary, and the left triangle region is not attributed to the carbon enrichment deposited by the bainite laths. After the test temperature fell from 723 K to 625.4 K (450 °C to 352.4 °C), a

cluster of sympathetic bainite nucleation occurred and grew in this triangle region (this process is pointed out by a green arrow in Figures 7(k) and (l)). This phenomenon of a 100 K (100 °C) temperature delay (from 723 K to 623 K (450 °C to 350 °C)) occurring in bainite nucleation and growth within an austenite grain is a characteristic of bainite transformation. It is considered to not be caused by the carbon enrichment deposited by the bainite laths, but by the nonuniform distribution in chemical compositions, which causes the difference in Gibbs free energy for phase transformation.

(3) Growth of bainite lath (sheaf) is by nucleation and growth of new subunits at the tip of existing subunits. In Figure 8, a bainite lath of Ni6-3 (held at 713 K (440 °C)) is formed by the successive nucleation and growth of subunit 1 at the tip of an existing bainite lath and then subunit 2 at the

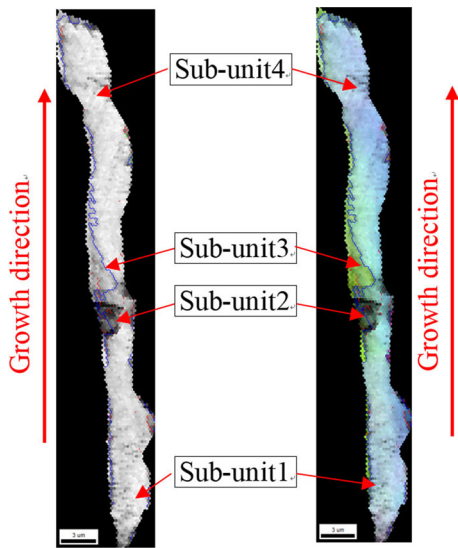


Fig. 8—Growth of bainite lath by nucleation and growth of new subunits at the tip of an existing subunit in a bainite sheaf.

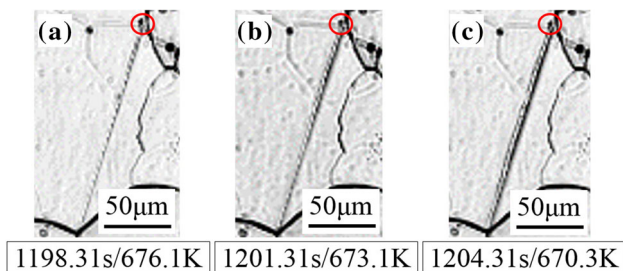


Fig. 9—Growth in the width of a bainite lath.

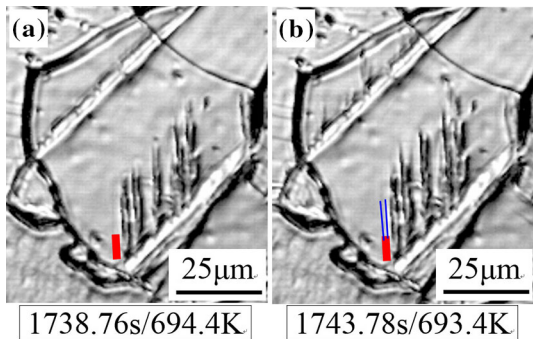


Fig. 10—Twin and branch growth of bainite lath—(a) primary bainite sheaf with twin laths indicated by red thick lines; (b) new laths indicated by blue thin lines and branches at the tip of bainite sheaf indicated by two black spikes.

tip of subunit 1, and tip of subunit 3 at the tip of subunit 2 and the tip of subunit 4 at the tip of subunit 3.

- (4) After lengthening, bainite lath widens at a very low rate. In Figure 9, it takes more than 6 seconds for a bainite lath (Ni7-2) to widen to about  $2\ \mu\text{m}$  (from 713 K to 710 K (400 °C to 397 °C)).

The widening rate of  $0.16\ \mu\text{m/s}$  is much lower than the lengthening rate ( $2\text{--}2000\ \mu\text{m/s}$ ). From Figures 9(a) through (c), the widening behavior seems to be caused by plastic deformation. It is worth noting that the widths of bainite laths are determined by the mode of nucleation. In cases where a number of bainite laths are sympathetically nucleated and grow in parallel, the widths of laths are not determined by the limit restricted by carbon deposition or phase transformation strain; rather they are determined by the interval between the nuclei.

- (5) Bainite laths grow in pairs and branch out at the tips. Here, this is referred to as twin and branch growth. Figures 10(a) and (b) are redrawn from a zoomed-in view of Figures 5(l) and (m) which were an observation of the Ni6-1 specimen cooled at 0.2 K/s. As shown in Figures 10(a) and (b), each bainite sheaf included twin laths (indicated by two blue short lines) and as the laths grew they branched out at the tips. The reason for the growth of bainite as twin laths in a sheaf is explained as for strain self-accommodation. Also, variants of laths belonging to the same Bain zone tend to be formed side by side at a slow cooling rate (0.2 K/s).<sup>[27]</sup> One of the branched tips then grows to a new lath.

#### E. The Kinetic Process Creating Bainitic Laths

Figures 11(a) through (h) depict the *in situ* observations of the morphological evolution of bainite laths in an austenite grain of the Ni6-3 specimen during isothermal holding at 713 K (440 °C). As shown in Figure 11(a), the first bainite lath (this lath is marked with 1) was nucleated at a defect void (this void is enclosed by a violet circle) and grew slowly (see Figure 11(b) at nearly  $4\ \mu\text{m/s}$ ). The second bainite lath (this lath is marked with 2) was attached at the lower side of the first nucleation site (Figure 7(c)) and grew rapidly (at  $700\ \mu\text{m/s}$ ) inclined to the first lath with a low angle (5 deg). The third bainite lath was nucleated at the broad side of the second lath, yet grew quite slowly (at merely  $2\ \mu\text{m/s}$ ) in a 60 deg angle inclined to the second lath (Figure 11(d)). The fourth bainite lath was nucleated 0.03 seconds later at the corner of the intersection of the second lath with the third lath and grew at  $1300\ \mu\text{m/s}$  in parallel with the first lath, leading to an angle slightly less than 60 deg between the third and the fourth laths (Figure 11(e)). As shown in Figures 11(a) through (f), it took 26.13 seconds for four bainite laths to finish nucleation and growth. Figure 11(f) shows the four laths reaching the grain boundary (thick black lines) and the morphology at the end of isothermal holding. In Figure 11(g), large even areas of untransformed austenite remain. Figure 11(h) displays the final morphology of the investigated grain after cooling, and it is found that the zones without surface relief become uneven. This phenomenon means that bainite transformation has occurred beneath the observation surface after cooling from 713 K (440 °C) to room temperature.

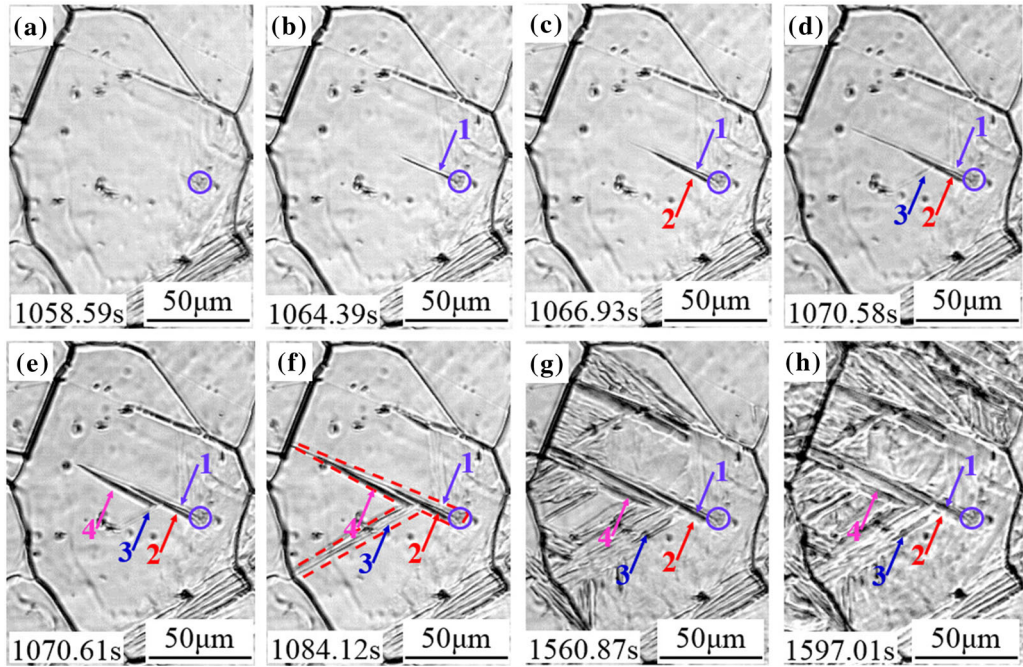


Fig. 11—(a through h) Morphological evolution of the Ni6-3 specimen during isothermal holding at 713 K (440 °C) for 10 min: The first nucleation site is indicated by the violet circle; the navy blue, red, dark blue, and violet arrows indicate the first, second, third, and fourth growing bainitic laths, respectively; the zone consisting of four laths is enclosed by red dotted lines in (f).

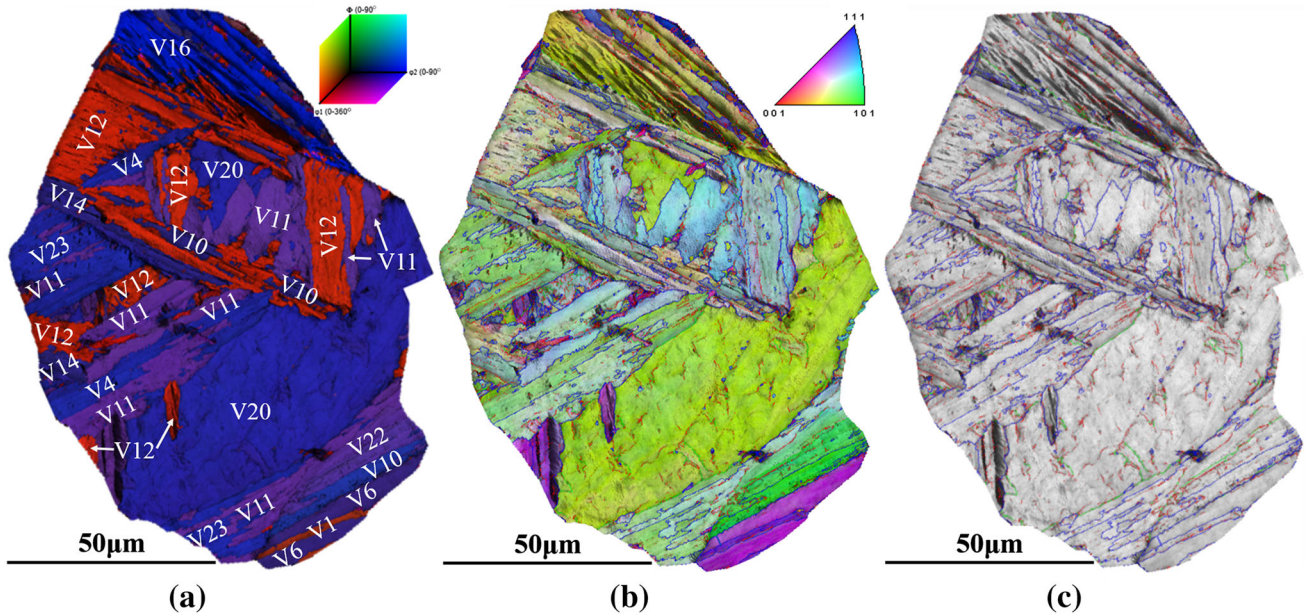


Fig. 12—(a) Euler figure (EF) color map of the investigated grain for identifying various variants—the symbols and numbers indicate the variant numbers; (b) inverse pole figure (IPF) color map of the investigated grains—colors of bainite variants in (a) and (b) correspond to the crystallographic orientations which are indicated in the inset stereographic triangle; (c) boundary figure (BF) revealed by EBSD: blue [15, 60 deg], green [5, 15 deg], and red [2, 5 deg].

It is well known that the K–S orientation relationship between austenite ( $\gamma$ ) and bainite ( $\alpha_b$ ) is expressed as  $(111)\gamma // (011)\alpha_b$ ,  $[\bar{1}01]\gamma // [\bar{1}\bar{1}1]\alpha_b$ . Twenty-four crystallographic variants can be formed and denoted as V1 to V24 which are summarized in Table III. Figure 12(a) shows an Euler figure (EF) color map of the formed bainite variants from the original austenite grain shown

in Figure 11(h). In accordance with the axis/angle pairs between diverse variants of the K–S orientation relationship reported by Morito *et al.*,<sup>[28]</sup> there are ten probable misorientation angles, *i.e.*, 10.53, 14.88, 20.61, 21.06, 47.11, 49.47, 50.51, 51.73, 57.21, and 60.00 deg, which are formed between different variants with variant V1, and all satisfy the K–S relationship as shown in

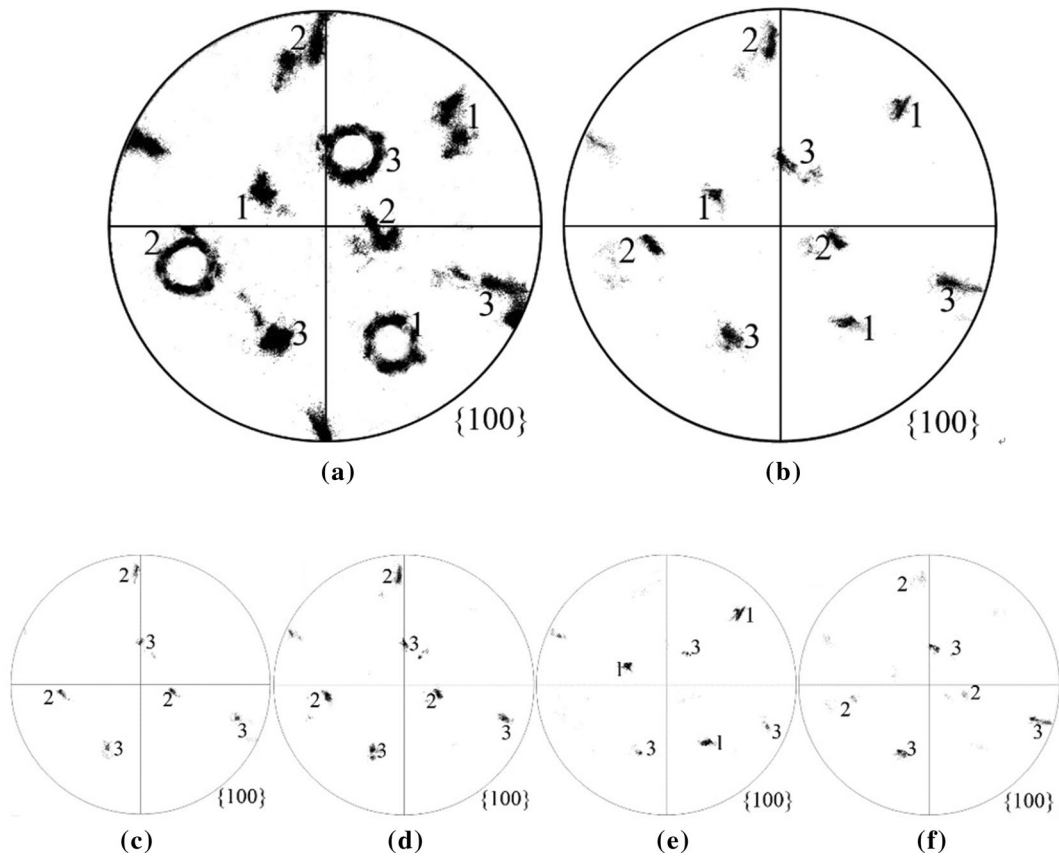


Fig. 13—(a through f)  $\{100\}_\alpha$  pole figures from the investigated grain, numbers refer to the three Bain zones for (a) the whole investigated grain, (b) four laths, (c) lath1, (d) lath2, (e) lath3, and (f) lath4.

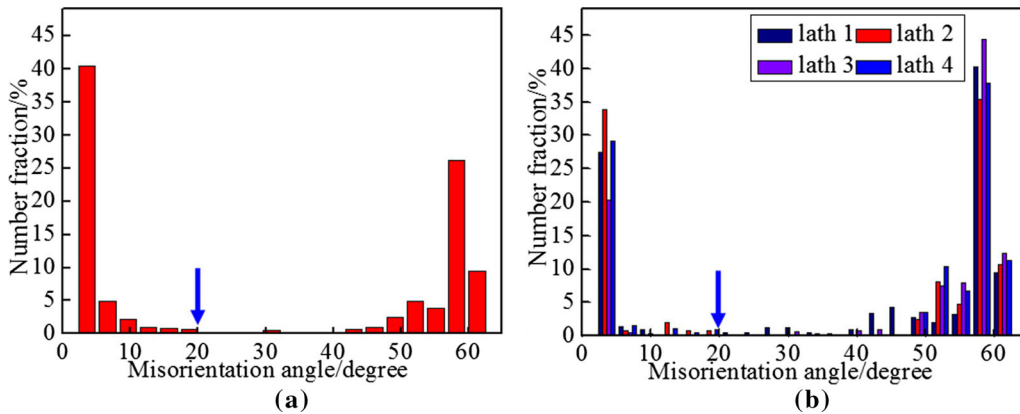


Fig. 14—(a) Histogram of misorientation angles between bainite sheaves within the investigated grain; (b) histogram of misorientation angles among four bainite laths.

Table III. In addition, the lowest threshold angle is experimentally estimated at 2 deg. Consequently, the boundaries are divided into three categories: low-angle boundaries with a misorientation of  $\theta < 5$  deg, medium-angle boundaries ( $5 \text{ deg} < \theta < 15 \text{ deg}$ ), and high-angle boundaries ( $\theta > 15 \text{ deg}$ ).<sup>[29]</sup> Because eight of ten probable misorientation angles between variants with V1 exceed 15 deg and even the lowest misorientation stays at a relatively large value of 10.53 deg, there must be large-angle boundaries for the adjacent bainite

variants formed with the K–S orientation relationship. Figure 12(a) displays the variants with various colors. Corresponding to the crystallographic orientation normal to the observation surface, the orientation of variants represented by the colors in Figure 12(a) is indicated by the stereographic triangle in the inset. The detailed morphology and crystallographic features of bainite structure are clearly shown in Figure 12(b). In Figures 12(b) and (c), the boundaries with different colors are drawn based on the misorientation between

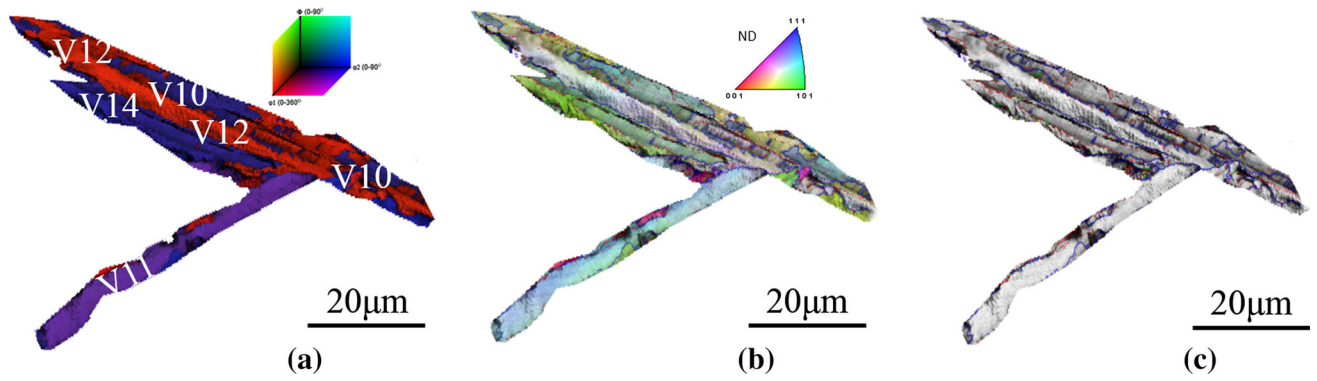


Fig. 15—(a) Magnified image of four laths in the EF map; (b) magnified image of four laths in the IPF map; and (c) magnified image of four laths in the BF map.

**Table IV. Four Typical Variants of K–S OR and Their Values for Bain Zones<sup>[27]</sup>**

Lath No.	Variant No.	Plane Parallel $(\gamma)//(\alpha)$	Direction Parallel $[\gamma]//[z]$	Bain Zone	Misorientation from V1 (deg)
1	V10	$(\bar{1}11)_{\gamma} // (011)_{\alpha}$	$[0\bar{1}1]_{\gamma} // [\bar{1}1\bar{1}]_{\alpha}$	B2	50.51
2	V12	$(\bar{1}11)_{\gamma} // (011)_{\alpha}$	$[101]_{\gamma} // [111]_{\alpha}$	B3	57.21
3	V11	$(\bar{1}11)_{\gamma} // (011)_{\alpha}$	$[101]_{\gamma} // [\bar{1}\bar{1}1]_{\alpha}$	B1	14.88
4	V14	$(\bar{1}11)_{\gamma} // (011)_{\alpha}$	$[110]_{\gamma} // [111]_{\alpha}$	B3	50.51

adjacent points of the EBSD data. As described above, three different criteria are used to draw the boundary: the blue lines indicate a misorientation larger than 15 deg, the green lines indicate that between 5 and 15 deg, and the red lines indicate that between 2 and 5 deg. Variant analyses of bainite in Figure 12(a) are shown in Figure 13. Figure 13 shows  $\{100\}$  pole figures depicting the orientation of the bainite crystals in the investigated austenite grain. They show (a) the whole investigated grain, (b) the four laths, (c) lath1, (d) lath2, (e) lath3, and (f) lath4. Three Bain zones are clearly visible as indicated by numbers in Figure 13(a). It is worth noting that our results are different from the view of Morito *et al.* who proposed that each packet contains the whole six variants.<sup>[28]</sup> Figure 14(a) demonstrates the misorientation angle histogram of bainite crystals within the investigated grain. As indicated in Figure 14(a), the theoretical peak around a misorientation angle of 20 deg (indicated with an arrow) was not observed in our experiment. This means that some variants disappear owing to variant selection during transformation, as reported by Lambert-Perlade *et al.*<sup>[30]</sup> This is especially true for the investigated grain shown in Figure 12(a) in which only 11 variants appear (V1, V4, V6, V10, V11, V12, V14, V16, V20, V22, and V23).

In Figures 11(a) through (h), the four laths, cropped out from the austenite grain, were designated as lath1, lath2, lath3, and lath4 in the order of growth sequence. Figures 15(a) through (c) show the EF image (variant distribution), IPF image (features of bainite structure), and BF image (high/low-angle grain boundary) of these four laths, respectively. The whole analysis process was the same as the process used for the austenite grain that was investigated in Figures 12(a) through (c). In the EF map (Figure 15(a)), lath1 contains V10 and V12, lath2 contains V12, lath3 contains V11, and lath4 contains V10

and V14. As shown in Table IV,<sup>[27]</sup> the misorientations of variants V10, V11, V12, and V14, from variant V1 are 50.51, 14.88, 57.21, and 50.51 deg, respectively. The IPF image in Figure 15(b) shows the detailed bainite structure features where four colors represent the involved orientations in Figure 15(a). The BF image in Figure 15(c) shows the high/low-angle grain boundary of the four laths in Figure 15(a). It is found that the blue curves representing misorientation >15 deg not only indicate packet boundary but also exist within laths. It can be observed from Figure 14(b) that the fraction of high-angle misorientation boundary in lath3 is the highest and the low-angle fraction is the lowest. In another research, it has been revealed that the growth rate of variants is influenced significantly by the fraction of high-angle misorientation in the bainite laths, that is, larger fraction of high-angle misorientation prohibits bainite growth.<sup>[28]</sup> This is considered to be one reason why the growth rate of the lath3 (2  $\mu\text{m/s}$ ) is apparently lower than those of lath4 (1300  $\mu\text{m/s}$ ) and lath2.

Consistent with the findings of Lambert-Perlade *et al.*, the crystallographic packets do not necessarily correspond to morphological packets.<sup>[30]</sup> Actually, crystallographic packets frequently consist of several morphological packets. In our experiment, the morphological packet was composed of lath1, lath2, and lath4 because the three laths present almost parallel lath morphology, while lath3 presents another morphology. However, lath1, lath2, and lath3 belong to one crystallographic packet because they (V10, V12, and V11 in Table III) all share the same habit plane  $(\bar{1}11)_{\gamma} // (011)_{\alpha}$ , while lath4 belongs to the other crystallographic packet. In sum, the laths belonging to one crystallographic packet will not necessarily grow in the same morphological direction. It is notable that the angle formed between lath3 and ‘lath1/ lath2’ reaches nearly 60 deg.

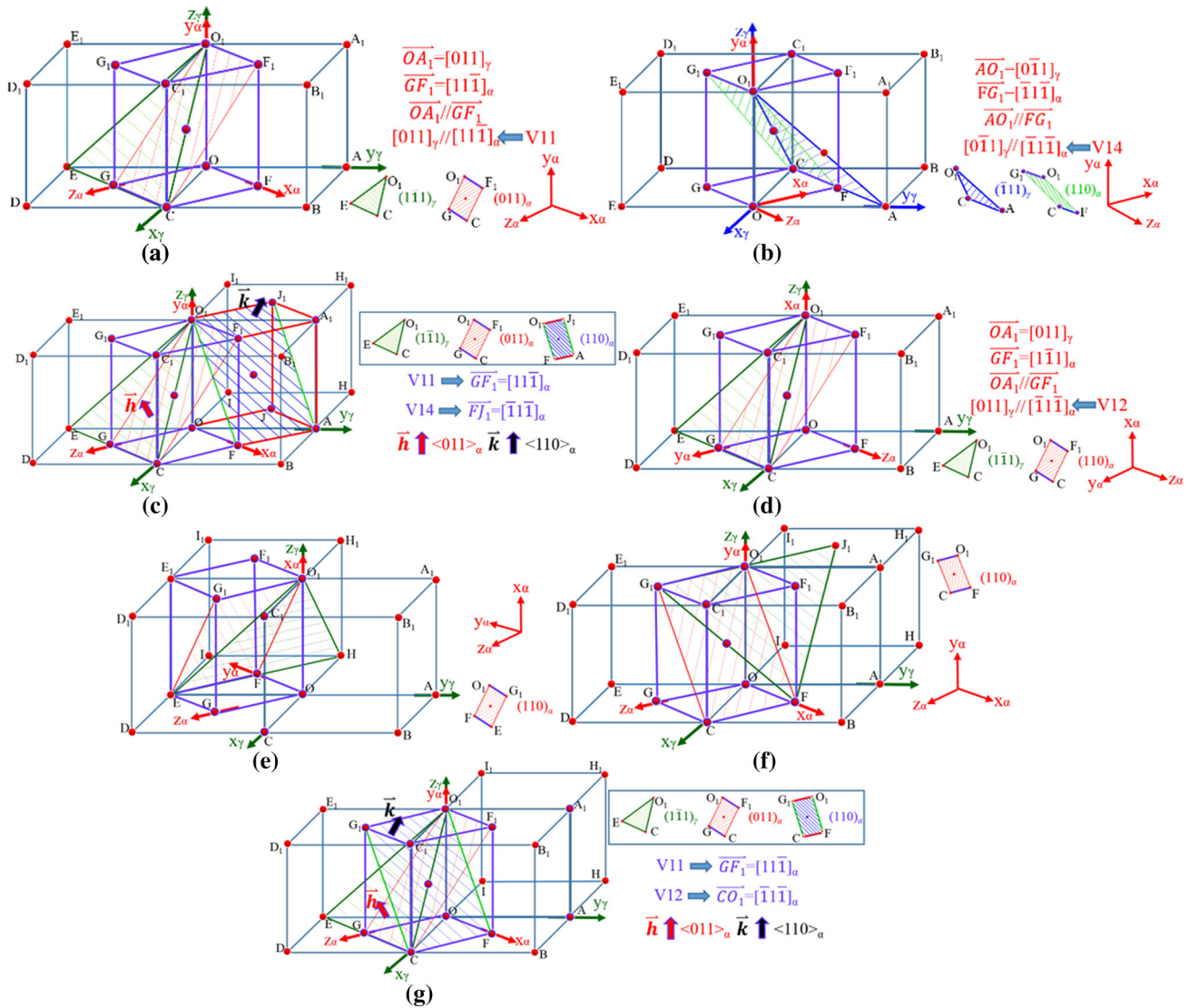


Fig. 16—(a through g) Lattice correspondence between FCC and BCC cells. (a) Lattice correspondence showing V11 ( $[101]_\gamma // [\bar{1}\bar{1}\bar{1}]_\alpha$ ); (b) lattice correspondence showing V14 ( $[110]_\gamma // [\bar{1}\bar{1}\bar{1}]_\alpha$ ); (c) integration of V11 and V14 under the identical Cartesian coordinate grid  $O-x_\alpha y_\alpha z_\alpha$ ,  $h$  and  $k$  representing the normal vectors of plane  $(011)_x$  and plane  $(110)_x$ , respectively; (d) lattice correspondence showing V12 ( $[011]_\gamma // [\bar{1}\bar{1}\bar{1}]_\alpha$ ); (e)  $O-x_\alpha y_\alpha z_\alpha$  through the counterclockwise rotation of 90 deg along the  $x_\alpha$ -axis in (e); (f) integration of V11 and V12 under the identical Cartesian coordinate grid  $O-x_\alpha y_\alpha z_\alpha$ ,  $h$  and  $k$  representing the normal vector of plane  $(011)_x$  and plane  $(110)_x$ , respectively.

This result is in accordance with the experimental phenomenon that an angle of nearly 50 deg is formed between two laths when the two corresponding variants belong to the same crystallographic packet.<sup>[31]</sup>

Figure 13(b) depicts a  $\{100\}_\alpha$  pole figure for all four laths and the numbers refer to three Bain zones. Figures 13(c) through (f) depict  $\{100\}_\alpha$  pole figures for lath1, lath2, lath3, and lath4, respectively. As shown in Figures 13(c), (d), and (f), variants in lath1, lath2, and lath4 are involved in Bain zone2 (B2) and Bain zone3 (B3), while variants in lath3 are involved in Bain zone1 (B1) and B3. The fact that only lath3 consisted of the subunits involved in B1 may be the second reason for the low growth rate of lath3.

Figure 16 depicts the lattice correspondence between FCC and BCC cells. In Figure 16(a), under the Cartesian coordinate grid  $O-x_\gamma y_\gamma z_\gamma$ , plane  $(\bar{1}\bar{1}\bar{1})_\gamma$  is shown by a

triangle filled with green lines, and plane  $(\bar{1}\bar{1}\bar{1})_\gamma$  is shown in Figure 16(b) by a triangle filled with blue lines. Likewise, under the Cartesian coordinate grid  $O-x_\alpha y_\alpha z_\alpha$ , plane  $(011)_\alpha$  is shown in Figure 16(a) by a rectangle filled with red lines, and plane  $(110)_\alpha$  is shown in Figure 16(b) by a rectangle filled with green lines. In Figure 16(a), lattice correspondence between  $\gamma_{fcc}$  structure (OCDE- $O_1C_1D_1E_1$ ) and  $\alpha_{bcc}$  structure (OFC-G- $O_1F_1C_1G_1$ ) occurs on the plane ( $O_1F_1GC$ ) where lath3 (V11) is nucleated, and in Figure 16(b) lattice correspondence between  $\gamma_{fcc}$  structure (OAB-C- $O_1A_1B_1C_1$ ) and  $\alpha_{bcc}$  structure (OFCG- $O_1F_1C_1G_1$ ) occurs on the plane ( $O_1G_1CF$ ) where lath4 (V14) is nucleated. Comparing Figures 16(a) and (b), it is notable that the Cartesian coordinate grid  $O-x_\alpha y_\alpha z_\alpha$  in Figure 16(b) is obtained after the Cartesian coordinate

grid  $O-x_\alpha y_\alpha z_\alpha$  in Figure 16(a) goes through the counter-clockwise rotation of 90 deg along the  $y_\alpha$ -axis. To be seen more clearly, the planes and directions in Figure 16(b) need to undergo the clockwise rotation of 90 deg along the  $y_\alpha$ -axis, as shown in Figure 16(c). The plane  $(110)_\alpha$  in Figure 16(b) is just the plane  $(110)_\alpha(O_1J_1AF)$  shown in Figure 16(c) by a rectangle filled with blue lines. Figure 16(d) depicts the lattice correspondence to show V12  $([011]_\gamma//[\bar{1}1\bar{1}]_\alpha)$ . Plane  $(\bar{1}\bar{1})_\gamma$  is shown in Figure 16(d) by a triangle filled with green lines, and plane  $(110)_\alpha$  is shown in Figure 16(d) by a rectangle filled with red lines. The planes and directions in Figure 16(e) are obtained after Figure 16(d) undergoes the clockwise rotation of 90 deg along the  $x_\alpha$ -axis. The planes and directions in Figure 16(f) are obtained after Figure 16(e) undergoes the clockwise rotation of 90 deg along the  $z_\alpha$ -axis, and finally the rotated  $O-x_\alpha y_\alpha z_\alpha$  in Figure 16(f) remains identical with that in Figure 16(c). Figure 16(g) depicts a combination of plane  $(110)_\alpha$  in Figure 16(f) and the structure in Figure 16(a) since these two figures possess the same Cartesian coordinate grids  $O-x_\gamma y_\gamma z_\gamma$  and  $O-x_\alpha y_\alpha z_\alpha$ . Comparing Figures 16(c) and (g), it is notably interesting that both V12 and V14 have the same habit plane  $(O_1J_1AF)$  and  $(O_1G_1CF)$ , although the two variants are not in the same crystallographic packet, but in the same Bain zone.

As shown in Figure 16(c), the normal vector of plane  $(011)_\alpha$  ( $O_1F_1GC$ ) is  $\bar{h}\langle 011\rangle$ , the direction lath3 (V11) grows. In the same way, lath4 (V14) is nucleated on the plane  $(110)_\alpha$  ( $O_1J_1AF$ ) and grows along  $\bar{k}\langle 110\rangle$ . After calculation, the angle between  $\bar{h}\langle 011\rangle$  and  $\bar{k}\langle 110\rangle$  is 60 deg and the dihedral angle between two nucleation planes is 120 deg. As it is well known that bainite grows in a three-dimensional space, the two growing bainite laths will emerge on the observation surface when the observation surface is parallel to the plane  $(\bar{1}\bar{1}\bar{1})$  made up of both  $\bar{h}\langle 011\rangle$  and  $\bar{k}\langle 110\rangle$ , and the angle of observed laths (between lath3 and lath4) is formed by the projection of two laths in the inner austenite grain at two directions ( $\bar{h}\langle 011\rangle$  and  $\bar{k}\langle 110\rangle$ ). As a result, the final angle between lath3 and lath4 is also nearly 60 deg. As mentioned previously, for example, the growth of both lath2 and lath4 can be regarded as an accumulation of subunits along the displacement vector  $\bar{k}\langle 110\rangle$  in B3. The high growth rates of lath2 and lath4 are considered to be caused by the favored orientation of growing  $(\bar{k}\langle 110\rangle)$  which produces the displacement vector being parallel to the surface.<sup>[32]</sup> However, compared with lath4, lath3 grows at a much lower rate, which is considered to be caused by the growing orientation  $\bar{h}\langle 011\rangle$  in B1 with a 60 deg included angle with  $\bar{k}\langle 110\rangle$  which produces the displacement vector inclined to the surface. Thus, it produces more phase transformation strain, which prohibits the growth of bainite laths. In addition, the crystal indices show the surface forming an acute angle with  $(\bar{1}\bar{1}\bar{1})$ , which offers a benefit for lath4 growth and hinders the growth of lath3. According to

Pak *et al.*,<sup>[32]</sup> the martensite start temperature of the interior is (100 K) 100 °C less than that of the surface, between which the  $\Delta G^{yz}$  (Gibbs free energy) difference is 729 J/mol. This energy stays in accordance with the strain energy of the elastically accommodated martensite plate.<sup>[33]</sup> Similarly, inner bainite lath growth due to a lack of  $\Delta G^{yz}$  needs to overcome the strain energy, which reduces its growth rate.

## IV. CONCLUSIONS

1. The features of relief produced by LSCM are able to display the microstructural morphology of bainite laths when viewed from various angles. Slim strips represent bainite laths growing perpendicularly to the polished surface, slightly wider strips represent bainite laths forming at an acute angle with the polished (free) surface, and darker and flatter facets represent the side of bainite laths parallel to the polished surface.
2. Five nucleation modes and six kinds of growth behavior were put forward.
3. Variants within one crystallographic packet being nucleated on the same habit plane can grow in different directions. Different laths grow at various rates although they belong to the same packet and the same Bain zone.
4. Bainite laths grow at a wide range of speed (from 2  $\mu\text{m/s}$  to higher than 2000  $\mu\text{m/s}$ ) as affected by (1) the density of the high-angle misorientation in it, (2) the included angle between habit planes of different variants, and (3) the direction of the displacement growing vector with respect to the free (polished) surface.

## ACKNOWLEDGMENTS

The authors are grateful to the National Nature Science Foundation of China (No. 51675255) for their financial support. Many thanks to Mr. Jesse Chaffin, Mr. Jeff Miles, Professor Nailing Sun, and Dr. Xiuli Mao for English language editing.

## REFERENCES

1. F.G. Caballero, H.K.D.H. Bhadeshia, K.J.A. Mawella, D.G. Jones, and P. Brown: *Mater. Sci. Technol.*, 2001, vol. 17, pp. 512–17.
2. H.K.D.H. Bhadeshia: *Mater. Sci. Technol.*, 2005, vol. 21, pp. 1293–302.
3. C. Garcia-Mateo and F.G. Caballero: *ISIJ Inter.*, 2005, vol. 45, pp. 1736–40.
4. H.K.D.H. Bhadeshia: *Bainite in Steels*, 2nd ed., Institute of Materials, London, 2001, pp. 146–148.
5. M.K. Kang, M.X. Zhang, and M. Zhu: *Acta Mater.*, 2006, vol. 54, pp. 2121–29.
6. X.M. Li and Z.Y. Xu: *Metallographic*, 1987, vol. 20, pp. 47–59.
7. H.J. Hu, G. Xu, Y.L. Zhang, Z.L. Xue, and M.X. Zhou: *J. Wuhan Univ. Technol.*, 2015, vol. 30, pp. 818–21.
8. D. Zhang, Y. Shintaku, S. Suzuki, and Y. Komizo: *J. Mater. Sci.*, 2012, vol. 47, pp. 5524–28.

9. F. Ishikawa and T. Takahashi: *ISIJ Inter.*, 1995, vol. 35, pp. 1128–33.
10. G. Xu, F. Liu, L. Wang, and H.J. Hu: *Scr. Mater.*, 2013, vol. 68, pp. 833–36.
11. D. Zhang, H. Terasaki, and Y.I. Komizo: *J. Alloys Compd.*, 2009, vol. 484, pp. 929–933.
12. X.F. Zhang, P. Han, H. Terasaki, M. Sato, and Y. Komizo: *J. Mater. Sci. Technol.*, 2012, vol. 28, pp. 241–48.
13. H. Yada and T. Ooka: *J. Jpn. Inst. Met.*, 1967, vol. 31, pp. 766–71.
14. P. Kolmskog, A. Borgenstam, M. Hillert, P. Hedstrom, S.S. Babu, H. Terasaki, and Y.I. Komizo: *Metall. Mater. Trans. A*, 2012, vol. 43A, pp. 4984–88.
15. B.L. Adams, S.I. Wright, and K. Kunze: *Metall. Trans. A*, 1993, vol. 24A, pp. 819–31.
16. H. Terasaki and Y. Komizo: *Metall. Mater. Trans. A*, 2013, vol. 44A, pp. 5289–93.
17. M. Sarizam and Y. Komizo: *J. Mech. Eng. Sci.*, 2014, vol. 7, pp. 1103–14.
18. G. Miyamoto, N. Takayama, and T. Furuwara: *Scr. Mater.*, 2009, vol. 60, pp. 1113–16.
19. T.J. Song and B.C. De Cooman: *Metall. Mater. Trans. A*, 2013, vol. 44A, pp. 1636–1705.
20. T. Ko and S.A. Cottrell: *J. Iron. Steel. Inst.*, 1952, vol. 172, pp. 307–12.
21. E. Swallow and H.K.D.H. Bhadeshia: *Mater. Sci. Technol.*, 1996, vol. 12, pp. 121–25.
22. E. Keehan, L. Karlsson, H.K.D.H. Bhadeshia, and M. Thuvander: *Mater. Charact.*, 2008, vol. 59, pp. 877–82.
23. C.J. Wu, G.L. Chen, and W.J. Qiang: *Metal Material Science*, 2nd ed., Metallurgical Industry Press, Beijing, 2000, pp. 3–12.
24. Z.Y. Xu, X.J. Jin, and J.H. Zhang: *Phase Transformation in Materials*, 1st ed., Higher Education Press, Beijing, 2013, pp. 87–99.
25. G.B. Olson and W.S. Owen: *New Aspects of Martensitic Transformations*, 2nd ed., Institute of Metals, Tokyo, 1976, pp. 105–10.
26. S. Zhang, N. Hattori, M. Enomoto, and T. Tarui: *ISIJ Inter.*, 1996, vol. 36, pp. 1301–09.
27. N. Takayama, G. Miyamoto, and T. Furuwara: *Acta Mater.*, 2012, vol. 60, pp. 2387–96.
28. S. Morito, H. Tanaka, R. Konishi, T. Furuwara, and T. Maki: *Acta Mater.*, 2003, vol. 51, pp. 1789–99.
29. A. Iza-Mendia and I. Gutierrez: *Mater. Sci. Eng. A*, 2013, vol. 561, pp. 40–51.
30. A. Lambert-Perlade, A.F. Gourgues, and A. Pineau: *Acta Mater.*, 2004, vol. 52, pp. 2323–37.
31. H. Terasaki, Y. Shintome, A. Takada, Y. Komizo, K. Moriguchi, and Y. Tomio: *Metall. Mater. Trans. A*, 2014, vol. 45A, pp. 3551–59.
32. J. Pak, D.W. Suh, and H.K.D.H. Bhadeshia: *Metall. Mater. Trans. A*, 2012, vol. 43A, pp. 4520–24.
33. H.K.D.H. Bhadeshia: *Bainite in Steels*, 2nd ed., Institute of Materials, London, 2001, pp. 120–23.